J Solid State Electrochem (2010) 14:1897–1907
DOI 10.1007/s10008-010-1020-1

ORIGINAL PAPER

# Corrosion behavior of Mg, AZ31, and AZ91 alloys in dilute NaCl solutions

**Lei Wang · Tadashi Shinohara · Bo-Ping Zhang**

Received: 2 October 2009 / Revised: 26 January 2010 / Accepted: 28 January 2010 / Published online: 2 March 2010
© Springer-Verlag 2010

**Abstract** Corrosion behavior of extruded Mg, extruded AZ31 alloy, and cast AZ91 alloy was investigated by electrochemical measurements in dilute NaCl solutions. Corrosion products and passivation films were analyzed by X-ray diffraction and X-ray photoelectron spectroscopy. All specimens exhibit the corrosion and passivation zones in dilute NaCl solutions. The aluminum content and alloy microstructure influence the corrosion and passivation processes. AZ91 alloy shows the broadest passivation zone followed by AZ31 alloy and Mg. AZ91 alloy reveals a highest corrosion resistance, and preferential attack is located at the primary Mg phase. Its relatively fine $\beta$-phase ($Mg_{17}Al_{12}$) network and $Al_2O_3/Al(OH)_3$ compounds produced on the passivation film are the main factors which limit the corrosion progress as compared with AZ31 alloy and Mg. The thick passivation product on AZ31 alloy is the key factor which restricts the corrosion attack in dilute solutions.

**Keywords** Magnesium and its alloys · Electrochemical measurements · Dilute NaCl solutions · Passivation · Pitting

L. Wang · B.-P. Zhang
School of Materials Science and Engineering,
University of Science and Technology Beijing,
Beijing 100083, China

L. Wang · T. Shinohara (✉)
Materials Reliability Center,
National Institute for Materials Science,
1-2-1 Sengen,
Tsukuba 305-0047, Japan
e-mail: SHINOHARA.Tadashi@nims.go.jp

## Introduction

Magnesium (Mg) and its alloys are used in different applications including automobile and computer parts, aerospace components, mobile phones, sporting goods, and household equipment because of their some advantageous properties. However, their poor corrosion resistance is one of the main properties that has hindered their widespread use in many applications, especially in marine environments, since it is the most electrochemically active metal used for structural purposes [1–6].

It is well known that the corrosion of magnesium/aluminum (Al) alloys in the media greatly depends on the aluminum content, microstructure, and environment including pH and chloride ion concentration [7–10]. Zhao et al. [11] have studied that a higher corrosion rate correlated with a higher chloride ion concentration at each pH value solution and correlated with a lower pH value for each chloride ion concentration solution on the corrosion of Mg alloy ZE41. In Wu′s study [12], a small current plateau in the anodic polarization curve was observed in a 0.5 wt.% NaCl solution whereas no current plateau occurred in the 3.5 and 5 wt.% NaCl solutions for AZ91D, AZCe2, and AZLa1 magnesium alloys. Meanwhile, the high frequency capacitive loop in the Nyquist plots decreased with increasing chloride concentration consistent with the decrease in the corrosion resistance with increasing chloride concentration.

Increasing the aluminum content in Mg–Al alloys has a beneficial influence on the corrosion behavior in chloride media [13], but the mechanism and the effect of aluminum still remain ill-refined. Al is partly in solid solution and precipitated in the form of $Mg_{17}Al_{12}$ along grain boundaries as a continuous phase as well as part of a lamellar structure for AZ91 alloy. Meanwhile, the distribution of $\beta$-phase

($Mg_{17}Al_{12}$) determines the corrosion resistance of Mg–Al alloys. Song et al. [14] have studied that the $\beta$-phase played a dual role in NaCl solutions. It served as a galvanic cathode and accelerated the corrosion process of the $\alpha$-matrix if the volume fraction of $\beta$-phase was small. On the other hand, the $\beta$-phase might act as an anodic barrier to inhibit the overall corrosion of the alloy for its high volume fraction. Raman et al. [15] found that an increase in the relative size of the $\beta$-phase at the expense of the Al-rich $\alpha$ area resulted in the greater localized corrosion due to the increase of cathode to anode area ratio. However, the existence of a surrounding Al-rich $\alpha$ area with independent electrochemical identity seemed to be dependent on the composition of the alloy. They were contradictory results depending on the aluminum content in the $\alpha$-phase. Pardo et al. [9, 10] reported that two key factors influenced the lowest corrosion rate of Mg–Al alloys, in which the aluminum enrichment on the corroded surface for AZ81 alloy and the $\beta$-phase acted as a barrier for the corrosion progress for AZ81 and AZ91D alloys. The galvanic coupling between the $\beta$-phase and the $\alpha$-matrix was not significant.

Most of the methods to understanding the corrosion mechanism of Mg–Al alloys employ alkaline solutions in order to the stability of the passivation layer [16, 17]. Very few of these studies have used the dilute chloride solutions. The corrosion behavior of AZ31 Mg alloy is insensitive to the atmospheric exposure environment reported by Shinohara et al. [18]. It means that the test coupons reveal a good resistance during raining, and it is necessary to provide the base for understanding alloy performance in dilute chloride solutions. In order to determine the corrosion behavior of Mg and its alloys in dilute NaCl solutions, in recent work, pure Mg, AZ31, and AZ91 alloys were studied on the basic of electrochemical measurements. The surface products were analyzed by X-ray diffraction (XRD) and X-ray photoelectron spectroscopy (XPS).

## Experimental

### Specimen preparation

Chemical compositions of the test materials, namely Mg, AZ31, and AZ91 alloys, are listed in Table 1. All materials were manufactured and supplied by Osaka Fuji Ltd. Mg and AZ31 alloy were used in the extruded shape of cylinder with dimensions of 8 mm ø×10 mm and 10 mm ø×10 mm. AZ91 alloy was supplied in the cast plate of a 20×5×5-mm ($l \times w \times t$) rectangular shape. Prior to electrochemical measurements, the test specimens were connected with lead wires and embedded in epoxy resins with only one of their surfaces left exposed. The exposed surface areas were 0.502 $cm^2$, 0.785 $cm^2$, and 1 $cm^2$ for Mg, AZ31, and AZ91 alloys, respectively. The exposed surfaces were mechanically polished up to 1,200-grit SiC paper, then polished with silica slurry, and finally rinsed with ethanol. The microstructures for metallographic analysis were etched in the reagents of Nital (5 mL $HNO_3$ + 95 mL ethanol) for Mg and AZ91 alloy and Vilella (0.6 g picric acid +10 mL ethanol + 90 mL $H_2O$) for AZ31 alloy during 10–15 s [10].

### Electrochemical measurements

The test solutions were subjected to aqueous solutions of 0.01–0.5 mol/L NaCl at room temperature. The open circuit potential ($E_{ocp}$) of the specimens was monitored in the test solutions for 72 ks using an SDPS-501C electrochemical analyzer (SYRINX Inc., Japan). Potentiodynamic polarization tests were performed using the SDPS-501C electrochemical analyzer from –1.70 to –1.3 V at a scanning rate of 0.17 mV/s in solutions at various concentrations. Potentiodynamic polarization tests were also performed by scanning the potential from –1.70 to –1.0 V at a rate of 0.17 mV/s in the 0.01 mol/L NaCl solution after different immersion times (3.6, 18, 36, and 72 ks) on $E_{ocp}$ measurement. Potentiostatic polarization tests were performed to observe the initiation and growth of pit using an SDPS-308 electrochemical analyzer (SYRINX Inc., Japan), in which the specimens were polarized immediately at a given potential after immersion and maintained at this potential for a given duration (3.6, 18, 36, and 72 ks). The same test was repeated at least twice for all specimens. A saturated calomel electrode and a 0.125-mm thick platinum foil (10×20 mm) were used as the reference electrode and the counter electrode, respectively.

### Morphology observation, XPS, and XRD analyses

The surface morphology of the specimens was characterized using a laser microscope (LM; VK-8500, KEYENCE

**Table 1** Chemical compositions of Mg, AZ31, and AZ91 alloys

| Material | Element | Content | wt.% | | | | | |
|---|---|---|---|---|---|---|---|---|
| | Al | Zn | Mn | Si | Cu | Ni | Fe | Mg |
| Mg | 0.003 | 0.006 | 0.0039 | 0.003 | 0.0003 | 0.0007 | 0.0047 | Balance |
| AZ31 | 3.05 | 0.82 | 0.40 | 0.020 | 0.003 | 0.0012 | 0.0023 | Balance |
| AZ91 | 8.80 | 0.71 | 0.19 | 0.029 | 0.002 | <0.001 | 0.001 | Balance |

Inc., Japan). The maximum pit depth was determined based on the depth profile measured by LM. For the investigation of maximum pit depth, the specimens were polarized potentiostatically in the solutions for 3.6, 18, 36, and 72 ks. For each polarization time, two replicas were used. The corrosion products on the surface were removed using a reagent of 5 g $Cr_2O_3$, 0.25 g $AgNO_3$, and 25 mL deionized water. Then the photography of one replica for each polarization time was scanned using LM. The microscope's lens were first focused on the lip of pit and then on the bottom of pit. Following the practice, every pit developed in the total immersed area of specimens was measured. The maximum pit depth was determined based on the values of 20–30 corrosion pits.

XPS (PHI Quantera SXM, ULVAC-PHI, Inc., Japan) was used for the surface chemical analysis. The X-ray source was monochromated Al K$\alpha$ radiation ($h\nu$ = 1,486.6 eV). Initial survey spectrum was obtained with the analyzer pass energy set at 280 eV. The take-off angle with respect to the surface was 45°. The sputtering rate was 1.84 nm/min. The surface products were analyzed by XRD (RINT-2500, Rigaku, Inc., Japan) using Cu K$\alpha$ radiation ($\lambda$ = 1.5416 Å) filtered through a Ni foil.

## Results

### Microstructure

Figure 1 shows the typical microstructures of the test specimens. Mg reveals equiaxial grains with a size of 20–50 μm. AZ31 alloy shows inhomogeneous cellular grains with the size of 5–40 μm. On the other hand, AZ91 alloy consists of a primary $\alpha$-phase, eutectic Mg phase, and $\beta$-phase. The eutectic Mg phase surrounded by $\beta$-phase is Al richer than primary $\alpha$-phase, and the $\beta$-phase is the discontinuous precipitate of intermetallic compound $Mg_{17}Al_{12}$, which are presented in the literature [3, 9].

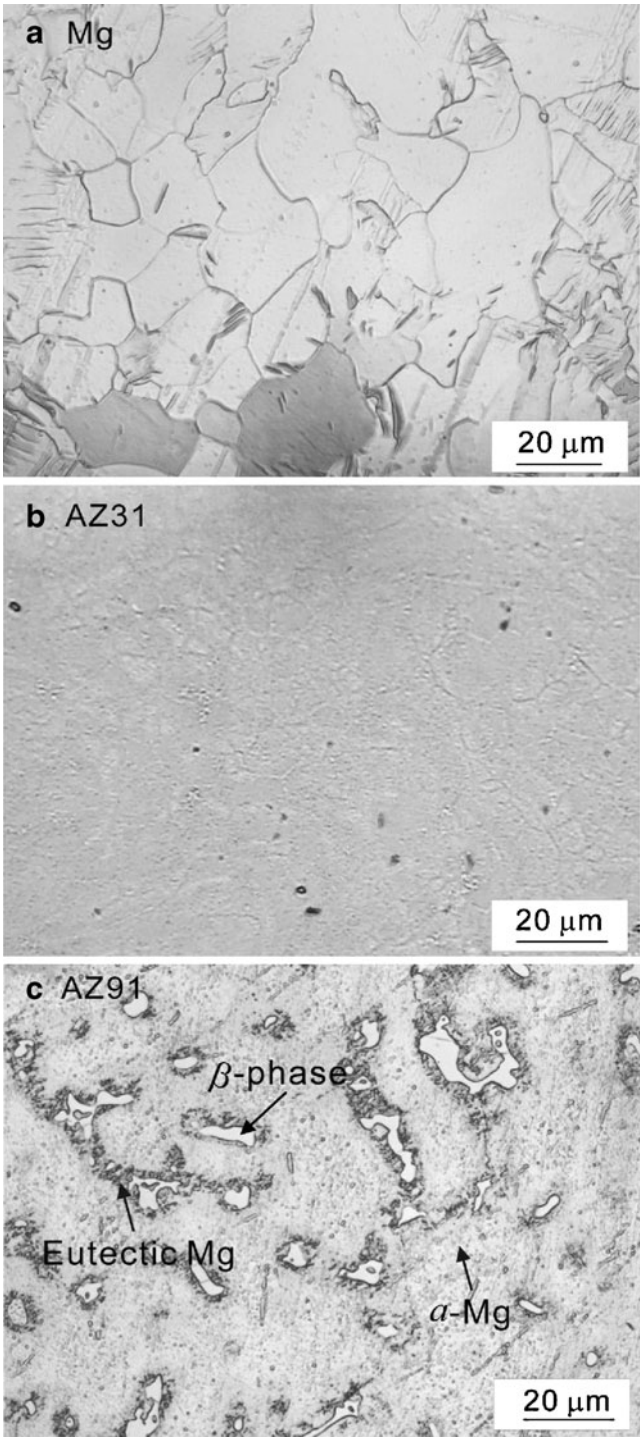


**Fig. 1** Microstructures of **a** Mg, **b** AZ31, and **c** AZ91 alloys

### Electrochemical measurements

Figure 2 shows the time variations of the $E_{ocp}$ for the test specimens in 0.01 and 0.1 mol/L NaCl solutions. The $E_{ocp}$ values initially increase quickly and then rise slowly in the 0.01 mol/L solution for all specimens, which are attributed to the stable growth of the protective surface films. On the other hand, in the 0.1-mol/L solution, the $E_{ocp}$ for Mg initially increases to a maximum and then decreases slowly with time (Fig. 2a). This behavior is ascribed to the dissolution of the surface film attacked by $Cl^-$ ion. The $E_{ocp}$ values for AZ31 and AZ91 alloys increase toward the nobler direction with frequent fluctuations after showing a rise and a drop (Fig. 2b). They indicate that the surface films formed with $Mg^{2+}$ and $OH^-$ ions were attacked by $Cl^-$ ion firstly and then passivated with the redeposited $Mg(OH)_2$ with increasing immersion time [19]. The fluctuations of $E_{ocp}$ might be due to the localized corrosion.

Figure 3 shows the polarization curves for the test specimens in the 0.01 mol/L NaCl solution. Mg and AZ31 alloys show the passivation region, and pits occurred after

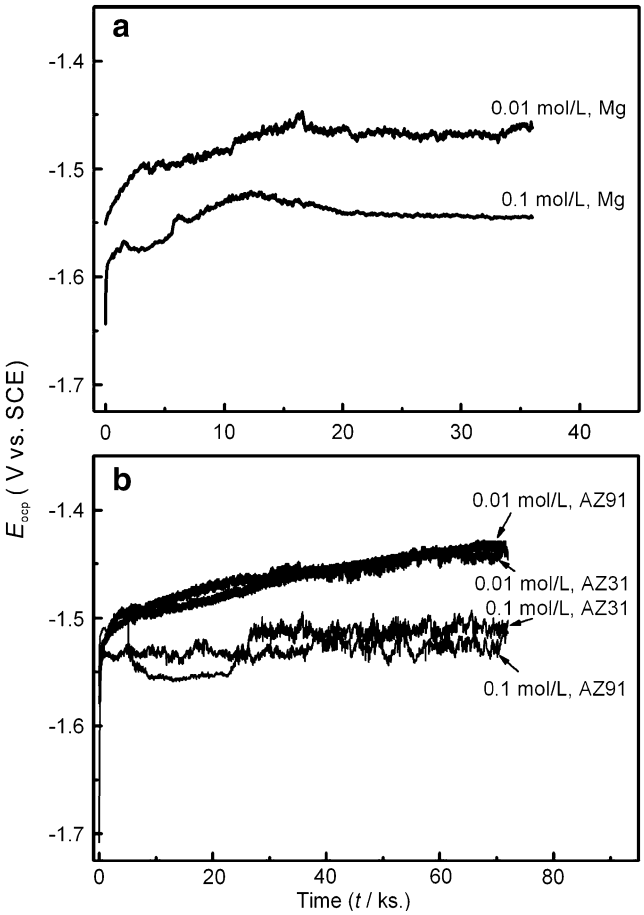


**Fig. 2** Time variations of open-circuit potentials for **a** Mg, **b** AZ31, and AZ91 alloys in 0.01 and 0.1 mol/L NaCl solutions for 72 ks (36 ks on Mg)

the current densities, $i$, rise up to 100 μA/cm$^2$. AZ91 alloy also exhibits the spontaneous passivation, and its passive current density is less than 50 μA/cm$^2$. However, pits appeared as $i$ rises up to 100 μA/cm$^2$. Therefore, the $V'_{c100}$ where $i$ reaches to 100 μA/cm$^2$ is taken as a pitting potential. Figure 4 summarizes the potential where $i$ is at 100 μA/cm$^2$ ($V'_{c100}$) for the test specimens in various concentrations NaCl solutions. The $V'_{c100}$ values decrease with increasing [Cl$^-$] for all specimens. The $V'_{c100}$ values of AZ31 and AZ91 alloys are higher than those of Mg, which reveal that the increased Al content and the formation of microstructure may be responsible for the higher $V'_{c100}$ in the formers. Additionally, the $V'_{c100}$ values of AZ31 alloy are higher than those of AZ91 alloy with increasing [Cl$^-$] from 0.03 to 0.5 mol/L, which are probably due to its more homogeneous microstructure of AZ31 alloy compared with AZ91.

Figure 5 shows the evolution of the polarization behavior of the test specimens in the 0.01 mol/L solution after the $E_{ocp}$ measurement. The corrosion potential ($E_{corr}$), corrosion current density ($i_{corr}$), and the passive current density ($i_{pass}$) at –1.40 V obtained from the curves are summarized in Fig. 6. All specimens reveal an obvious shift of $E_{corr}$ toward more noble value and a decrease of passive current density with increasing immersion time. It may be due to the nucleation and growth of a thick and semi-protective layer of corrosion products reported by Pardo et al. [9]. The Tafel extrapolation method measures the Mg corrosion rate, and the $i_{corr}$ is estimated by Tafel extrapolation of the cathodic branch of the polarization curve. The $i_{corr}$ (milliampere per square centimeter) can be related to the corrosion rate, $P_i$ (millimeter per year), using the following conversion equation [20–23].

$$P_i = 22.85 i_{corr} \quad (1)$$

Table 2 presents the corrosion rate, $P_{io}$ (evaluated from the $i_{corr}$ from polarization curves for freshly prepared specimens), compared with the corrosion rate, $P_{iss}$ (evalu-

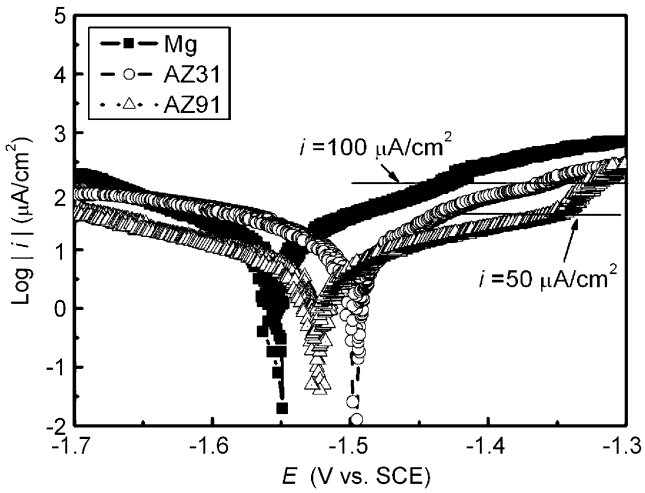


**Fig. 3** Polarization curves for Mg, AZ31, and AZ91 alloys in 0.01 mol/L NaCl solution

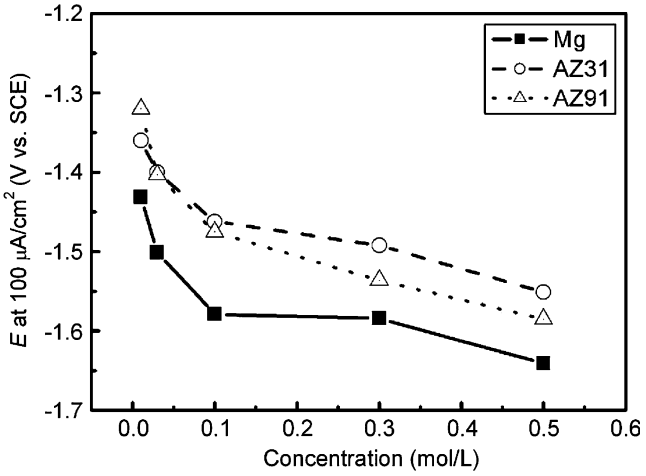


**Fig. 4** The potential where the current density reaches to 100 μA/cm$^2$ in the anodic polarization curves of Mg, AZ31, and AZ91 alloys in various concentrations NaCl solutions, respectively

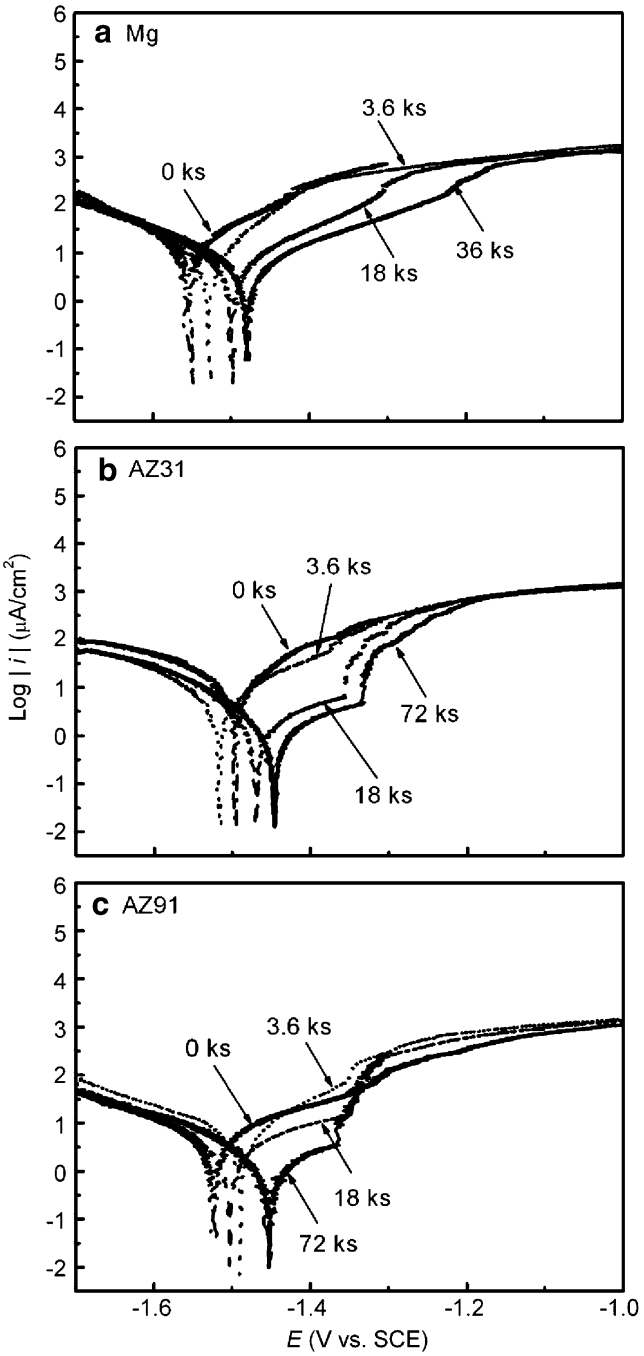


**Fig. 5** Influence of immersion time on $E_{ocp}$ measurement on the polarization behavior for **a** Mg, **b** AZ31, and **c** AZ91 alloys in 0.01 mol/L NaCl solution

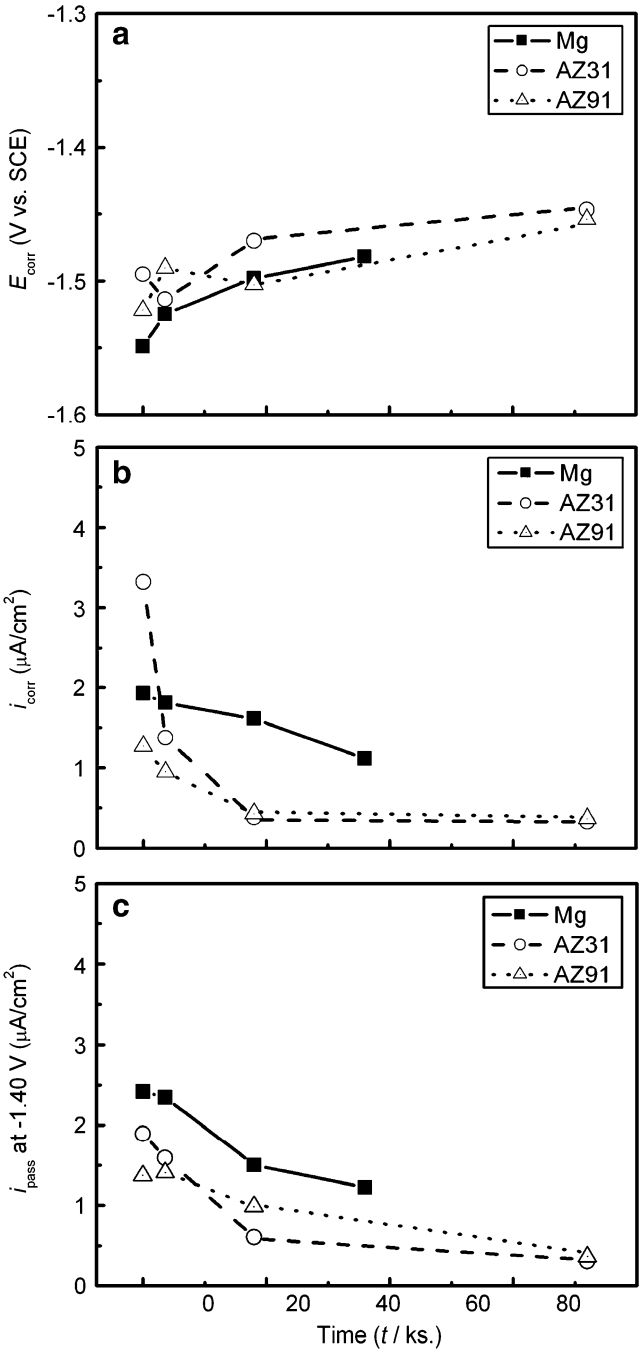


**Fig. 6** Influence of immersion time on $E_{ocp}$ measurement for Mg, AZ31, and AZ91 alloys in 0.01 mol/L NaCl solution on **a** corrosion potential ($E_{corr}$), **b** corrosion current density ($i_{corr}$), and **c** passive current density ($i_{pass}$) at –1.40 V

ated from the $i_{corr}$ from polarization curves for specimens after the $E_{ocp}$ measurement), for the test specimens in the 0.01 mol/L NaCl solution. The $P_{iss}$ values decrease with time, and therefore, a better corrosion behavior is exhibited for AZ31 and AZ91 alloys. The $P_{iss}$ values on AZ31 and AZ91 alloys are lower than those on Mg. AZ31 presents the most significant change on the $P_{io}$ and $P_{iss}$. It is possibly due to the high reactivity of this material which promotes the formation of a thick passivation layer, limiting the attack progression.

Figure 7 shows the typical time variations of the current densities for the test specimens polarized potentiostatically in the 0.01 mol/L NaCl solution at various potentials within the range of the $E_{corr}$ (–1.55 ~ –1.50 V) and the $V'_{c100}$ (–1.32 ~ –1.44 V). These curves can be categorized into

**Table 2** Corrosion rate, $P_{io}$ (evaluated from the $i_{corr}$ from polarization curves for freshly prepared specimens), compared with the corrosion rate, $P_{iss}$ (evaluated from the $i_{corr}$ from polarization curves measured for specimens after the $E_{ocp}$ measurement at various time), for Mg, AZ31, and AZ91 alloys in 0.01 mol/L NaCl solution

| Material | $P_{io}$ (mm/year) | | $P_{iss}$ (mm/year) | | |
|---|---|---|---|---|---|
| | 0ks | 3.6ks | 18ks | 36ks | 72ks |
| Mg | 0.04 | 0.04 | 0.04 | 0.03 | |
| AZ31 | 0.08 | 0.03 | 0.01 | | 0.01 |
| AZ91 | 0.03 | 0.02 | 0.01 | | 0.01 |

three stages. The stage I is attributed to the initially increased and decreased $i$, in which small pits occurred and were observed following this active period. The stage II is attributed to the low $i$ below 100 μA/cm$^2$ showing the passivation. The stage III is owed to the high $i$ above 100 μA/cm$^2$ meaning the corrosion, which is caused by the dissolution of the performed passivation film.

## Corrosion morphology and pit depth

Figure 8 shows the micrographs of the test specimens polarized potentiostatically in the 0.01 mol/L NaCl solution at various potentials and times. The potentials were chosen in stage III for Mg at –1.45 V, AZ31 at –1.40 V, and AZ91 at –1.35 V, as shown in Fig. 7. In the initial stage of 3.6-ks polarization, Mg and AZ31 alloys show both the pitting and filiform-like corrosion. The filiform of corrosion seems like the corrosion of magnesium alloys reported by Lunder [24] and Lindström [25, 26]. AZ91 alloy exhibits the pitting corrosion that occurred in the edge of $\beta$-phase which may form a galvanic couple with the surrounding Mg matrix. After 18-ks polarization, all specimens are covered with localized corrosion by the coalescence of pit and filiform. It seems that the rate of pit growth increases with time, yielding a rough-etched surface with large pits, and therefore, intense pitting result. Although AZ31 alloy reveals a higher corrosion resistance than Mg, its surface is completely covered by the thick and uneven corrosion products after 3.6-ks polarization. In agreement with the electrochemical measurements, AZ91 alloy reveals the less corrosion damage, and large areas are not affected even after 72-ks polarization.

Figure 9 shows the time variations of the maximum pit depths for the test specimens, polarized potentiostatically in the 0.01 mol/L NaCl solution at various potentials. The pit depths on AZ31 at –1.44 V and AZ91 at –1.40 V show a quick increase with 3.6-ks polarization and then almost keep a steady value from 18- to 72-ks polarization. Mg at –1.50 V shows a slight change in depth which means the metastable pit forming on the surface. On the other hand,

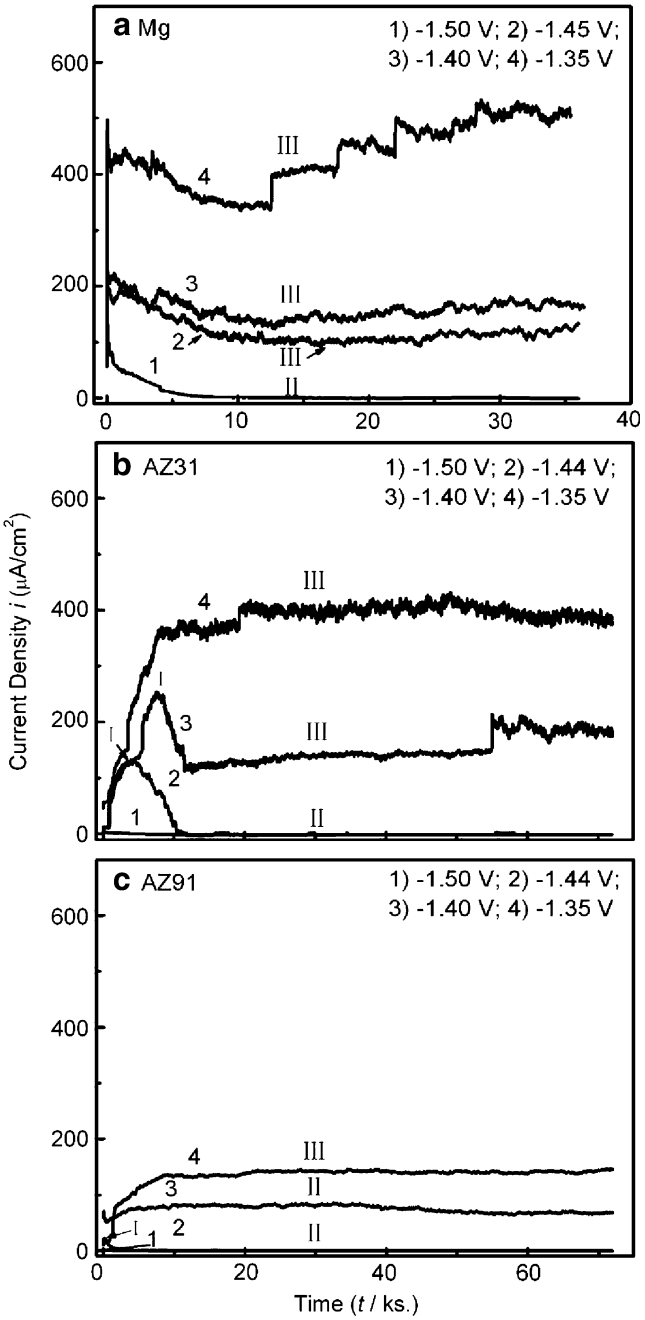


**Fig. 7** Time variations of current densities on **a** Mg, **b** AZ31 [19], and **c** AZ91 alloys polarized potentiostatically in 0.01 mol/L NaCl solution at various potentials for 72 ks (36 ks on Mg; I, II, and III represent pit, passivation, and corrosion states, respectively)

the pit depths on AZ31 at –1.40 V and AZ91 at –1.35 V show a quickly increasing trend within 3.6-ks polarization and then a slow rise until 72-ks polarization. The depth on AZ31 increases from 15 to 25 μm and that on AZ91, changes from 9 to 17 μm in spite of the low corrosion rate after 18-ks polarization. The pit depth on Mg at –1.45 V increases quickly to 31 μm within 3.6-ks polarization and rises continuously to 40 μm until 18-ks polarization. After

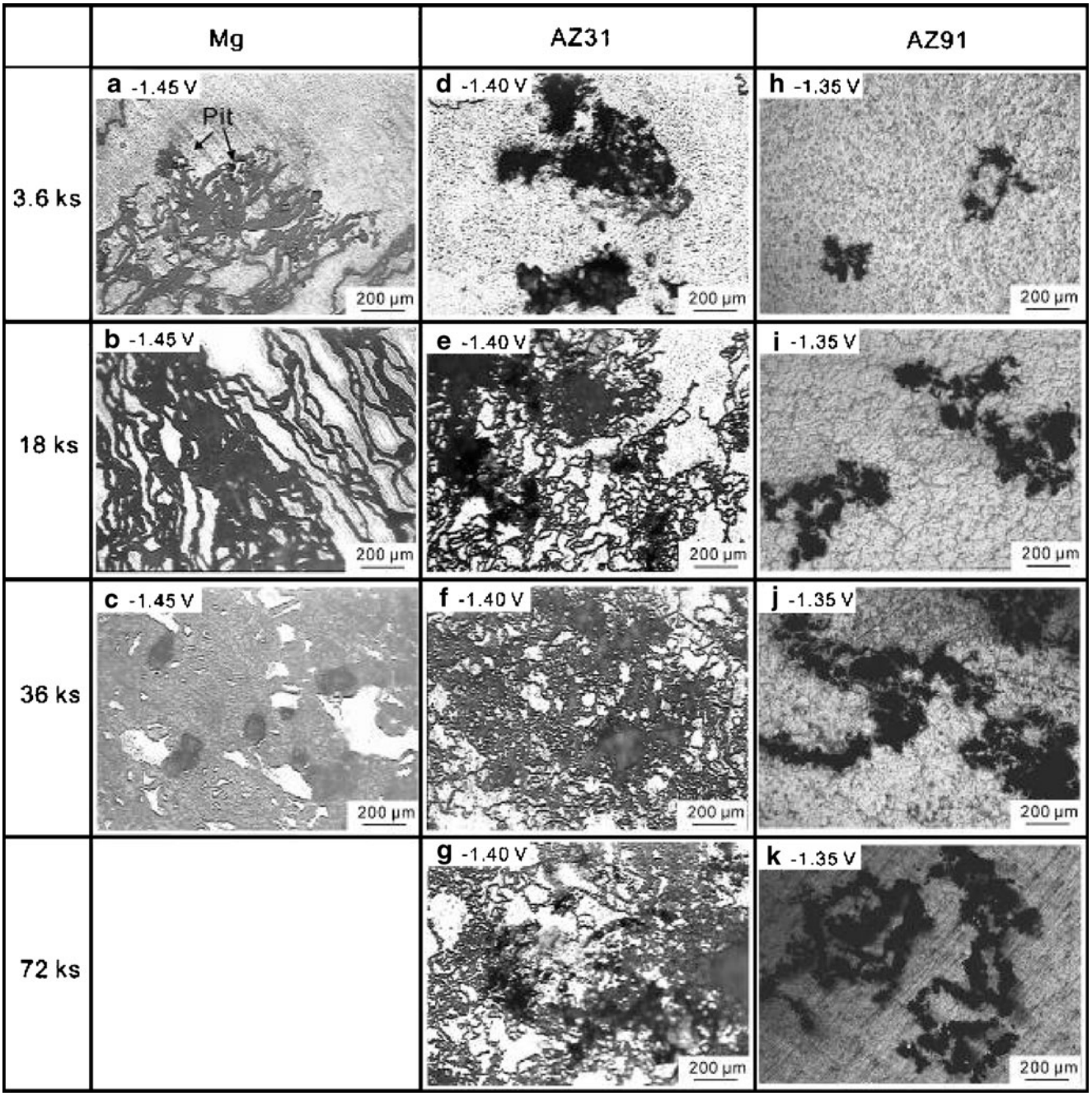


**Fig. 8** Laser micrographs of test specimens polarized potentiostatically in 0.01 mol/L NaCl solution for 72 ks at the following potentials: **a–c** –1.45 V on Mg; **d–g** –1.40 V on AZ31; **h–k** –1.35 V on AZ91

36-ks polarization, most parts were dissolved in the solution. It thus presents the most significant change on the depth value as compared with AZ31 and AZ91 alloys, which is due to the poor corrosion resistance and the high dissolution of Mg without the Al content. Since the continuous increase in pit depth for Mg, AZ31, and AZ91 alloys polarized at –1.45 V, –1.40 V, and –1.35 V, these potentials are considered as the critical pitting potentials ($V_c$) for the propagation of pit in the 0.01-mol/L solution.

## Corrosion map

Figure 10 shows the corrosion maps for the test specimens obtained in terms of electrode potential and [$Cl^-$] according to the results of electrochemical measurements and morphology examinations. All specimens exhibit the corrosion and passivation zones in dilute chloride solutions. Mg exhibits the smallest passivation zone as compared with AZ31 and AZ91 alloys. The $E^0_{ocp}$ were

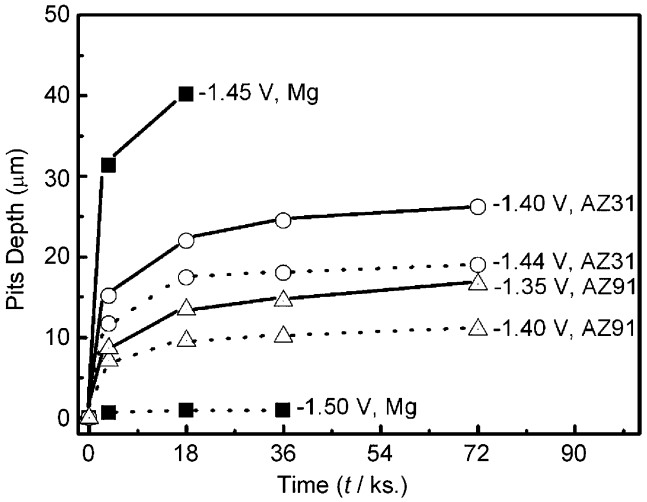


**Fig. 9** Time variations of pit depths on Mg, AZ31, and AZ91 alloys polarized potentiostatically in 0.01 mol/L NaCl solution at various potentials

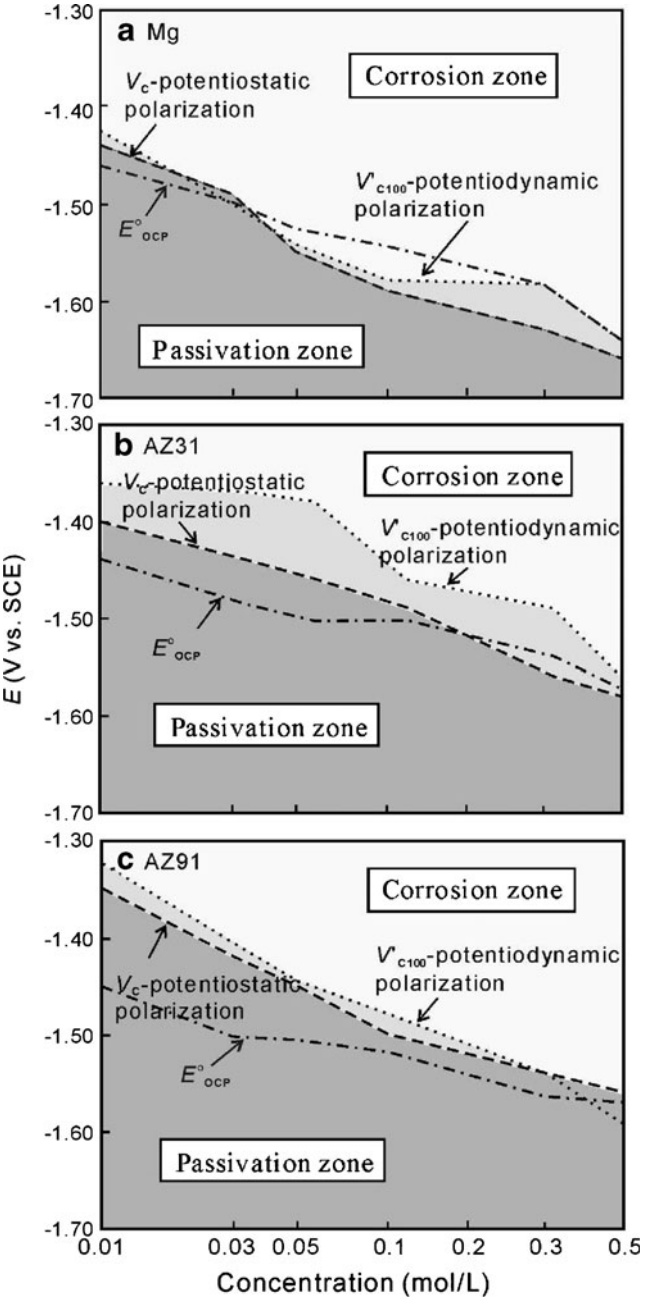


**Fig. 10** Corrosion maps of **a** Mg, **b** AZ31, and **c** AZ91 alloys in diluted NaCl solutions, in which corrosion and passivation zones correspond to electrochemical measurements

determined as $E_{ocp}$ values after immersion 36 ks on Mg and 72 ks on AZ31 and AZ91 alloys in solutions, respectively. $V'_{c100}$ were obtained from potentiodynamic polarization tests, and $V_c$ were determined by potentiostatic polarization tests. The $V_c$ values are almost lower than the $V'_{c100}$ ones. The $V_c$ are the main boundaries which divide the corrosion and passivation zones and shift to the negative direction accompanied with the passivation zone becoming narrow with increasing [$Cl^-$] for all specimens. Meanwhile, the $E_{ocp}{}^0$ are in the passivation zone when [$Cl^-$] are less than 0.05, 0.2, and 0.5 mol/L on Mg, AZ31, and AZ91 alloys, respectively.

## XRD and XPS analyses

Figure 11 shows the XRD patterns of the test specimens, polarized potentiostatically in the 0.01 mol/L solution in corrosion and passivation zones. All the characteristic peaks originate from the metallic Mg substrate. The $\beta$-phase ($Mg_{17}Al_{12}$) is found in AZ91 alloy. Mg reveals the presence of $Mg(OH)_2$ and $MgCO_3{\cdot}2H_2O$ phases in the corrosion zone, while the $Mg_2CO_3(OH)_2{\cdot}0.5H_2O$ phase in the passivation zone (Fig. 11a). AZ31 and AZ91 alloys show the same phases in both zones, in which $Mg(OH)_2$, $Mg_5(CO_3)_4(OH)_2{\cdot}5H_2O$, and MgO phases are found in the corrosion products and the latter two phases existed in the passivation films (Fig. 11b, c). The evidence of carbonates in the surface products is possibly due to the dissolution of atmospheric $CO_2$.

Figure 12 shows the depth profiling of Al 2p for AZ31 and AZ91 alloys in the 0.01 mol/L NaCl solution in the passivation zone. AZ31 alloy (Fig. 12a) shows the relatively obvious signal at 76.0±0.1 eV representing $Al_2O_3$ and $Al(OH)_3$ after 5-min sputtering time. AZ91 alloy (Fig. 12b) exhibits the stronger signal of metallic Al and aluminum compounds with increasing sputtering time from 1 to 35 min. The lower binding energy peak at 75.0 eV shifts to the higher one at 75.9 eV with time, accompanying with a clear shoulder peak at 72.7 eV owing to metallic Al existed in the 35-min sputtering time.

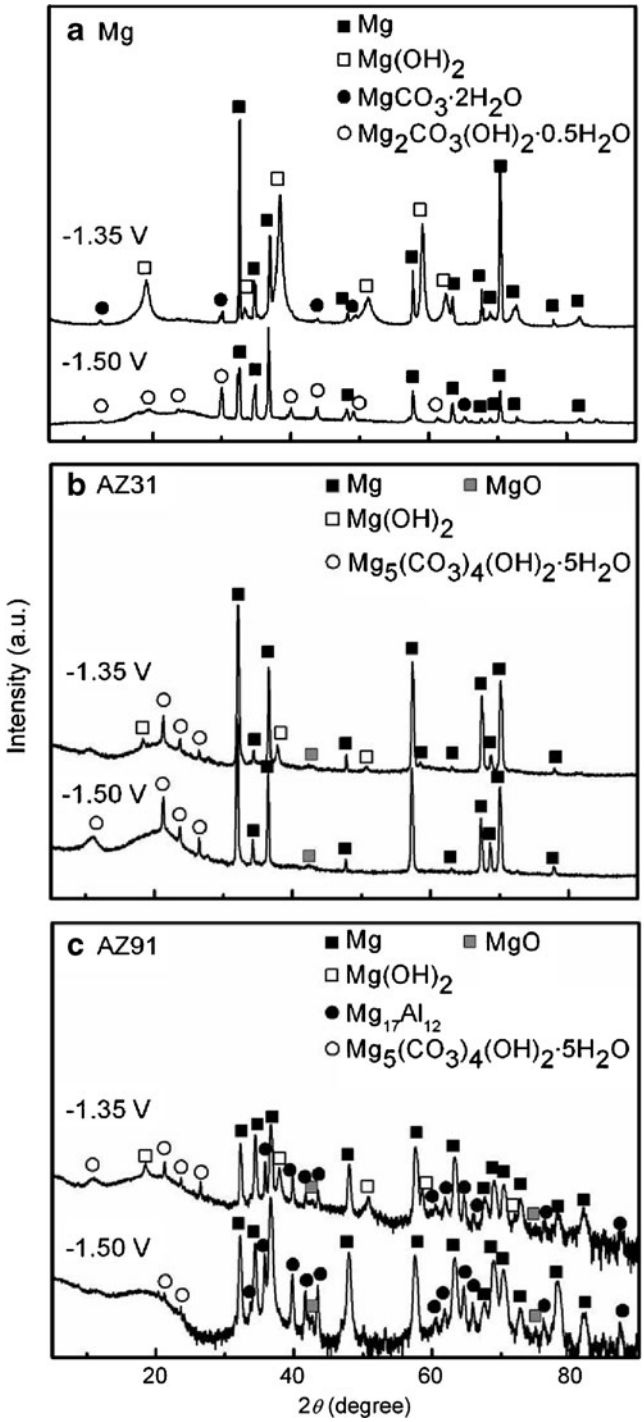


**Fig. 11** XRD patterns for **a** Mg, **b** AZ31, and **c** AZ91 alloys polarized potentiostatically in 0.01 mol/L NaCl solution at –1.35 V (in corrosion zone) and at –1.50 V (in passivation zone) for 72 ks (36 ks on Mg)

## Discussion

In general, the criteria for pit nucleation are the presence of an aggressive ion and passive overall state in the metal. Pit nucleation and metastable pit occur at potentials far below the pitting potential, and thus, their formation cannot be correlated to the pitting potential [27]. In this study, two metastable pits in the passivation zone were investigated. One metastable pit is nucleated as the $i$ is near the 0–10 μA/cm$^2$. This is indicated by the active AZ31 and AZ91 alloys, in which the $i$ increased initially while applying a potential of –1.50 V. The metals are then passivated by the growth of surface films of increasing thickness while the $i$ value quickly decreased up to 0–10 μA/cm$^2$ (Fig. 7b–c). The other metastable pit is initially nucleated, propagated, and passivated, following by a growth termination stage and with the surface products covering over the pit. This can be seen from the AZ31 alloy, which is shown to be active with initially increased $i$ while applying a potential of –1.44 V. After 10.8-ks polarization, the metal is passivated by the growth of corrosion products (Fig. 7b). This leads to the hindrance of the current density flowing through the pit and thereby, significantly reduces the relatively high $i$ after a long period of polarization (10.8 ks). Moreover, for relatively high $i$ (>50 μA/cm$^2$) flowing on the surface for AZ91 at –1.40 V (Fig. 7c), corrosion expands to horizontal direction, and the corroded areas are very shallow based on the morphology observation (Fig. 9). The corrosion state under those conditions is thus determined in the passivation zone.

Once the pitting potential is reached, pit growth begins on the surface of some small spots, and the $i$ value across these areas is under the influence of metal dissolution, instead of the passivation film growth. Pit grows at a fast rate in these pit regions and thus resulting in relatively high $i$ value [27]. In the potentiodynamic polarization, $V'_{c100}$ is taken as a parameter to evaluate the corrosion attack since it is difficult to define the pitting potential due to the unstable $i$ increase (Fig. 4). In the case of potentiostatic polarization, $V_c$ is defined as the critical pitting potential for pit nucleation and propagation for the increased pit growth value of up to 72-ks polarization (Fig. 10). The surface is partitioned into two different zones: the pitting zone conducting a high $i$ and the passivation zone conducting a relatively much lower $i$. Some of the film growth current, which existed prior to the start of pitting, must be diverted from the passivation part into the pitting part of the surface. Moreover, above the $V_c$, the surface areas and the pit depths grow with time, leading to localized corrosion.

Correlating with the corrosion maps for Mg and its alloy (Fig. 10), the shift in $V_c$ values toward less noble potentials is related to the greater activity of the materials with increasing [Cl$^-$]. It is likely that magnesium chloride or hydroxide produces a film defect which enables an easier ingress of aggressive Cl$^-$ anion [2, 3, 28]. That would undoubtedly lead to an increase in the pitting susceptibility, in agreement with the corresponding shift in

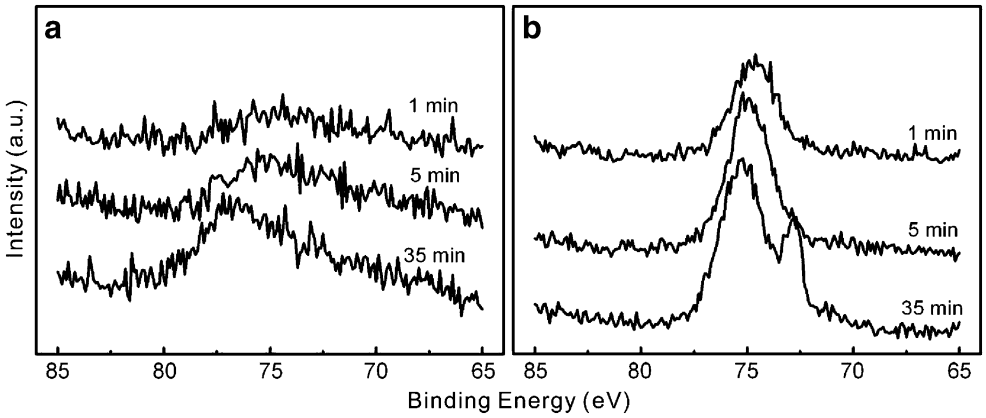


**Fig. 12** Depth profiling of Al 2p XPS spectra obtained from **a** AZ31 and **b** AZ91 alloys polarized potentiostatically in 0.01 mol/L NaCl solution at –1.44 V for 72 ks

the $E^0_{ocp}$ to more negative values as the solution concentration is increased. The $E^0_{ocp}$ values in the passivation zone indicate that the surface films or the corrosion products covering the material may play a protective layer and retard the further corrosion in dilute chloride solutions.

Considering the compositions of materials, the applied potential showing the passivation enhances with the alloyed Al content (Figs. 7 and 10). For instance, the potential in stage III for AZ91 alloy is higher than that for Mg and AZ31 alloy in the 0.01 mol/L NaCl solution. This reveals a growing tendency that the rate of passivation dominates over the rate of metal dissolution with increasing Al content in the magnesium, leading to the higher potential in the corrosion state. Meanwhile, it is attributed to the general weakness and the thinning of the passive film as a result of the aggressive attack of $Cl^-$ anion following its adsorption. This adsorption is expected to enhance as the applied potential becomes increasingly positive. These results confirm that the rate of pit nucleation depends on the applied potential, suggesting the coexistence of nucleation sites with different energies, each of which nucleates at distinct potentials [29].

AZ91 alloy is found to contain the least corrosion damage and the broadest passivation zone as compared to Mg and A31 alloy (Figs. 8 and 10). The presence of the relatively fine $\beta$-phase network segregated in the matrix alloy (Fig. 1c) may act as an effective barrier against progression of corrosion attack. In addition, the Al 2p spectra indicate the stronger signals of metallic Al and aluminum compounds in the passivation zone (Fig. 12), likely representing one of the main reasons for the improved corrosion resistance exhibited by the Al-rich components coming from the Mg substrate. Baliga et al. [13] reported that the presence of aluminum in single-phase Mg–Al alloys had a beneficial effect on the corrosion behavior in the chloride media. Nordlien et al. [30] also indicated aluminum enrichment in the oxide layer of Mg alloy exposed to humid air, which was believed to provide a better passivation of the surface by the formation of an alumina continuous skeletal structure. It thus confirms that the different distribution of alloying elements and microstructure influence the corrosion morphology and corrosion resistance of Mg alloys.

## Conclusions

1. Corrosion maps in terms of the electrode potentials and the [$Cl^-$] for extruded Mg, extruded AZ31 alloy, and cast AZ91 alloy were obtained using electrochemical measurements. The specimens exhibit the corrosion and passivation zones in dilute NaCl solutions. The open circuit potential values ($E^0_{ocp}$) are in the passivation zone when [$Cl^-$] are less than 0.05, 0.2, and 0.5 mol/L on Mg, AZ31, and AZ91 alloys, respectively.
2. The corrosion attack of Mg and its alloy in dilute chloride solutions depends on both Al content and alloy microstructure. An increase of the Al content in the composition of the alloys reduces the activity of Mg in dilute chloride solutions. For the AZ31 alloy, 3 wt.% Al reduces the corrosion susceptibly compared with Mg. AZ91 alloy exhibits a better corrosion resistance in all specimens.
3. AZ31 alloy has a good corrosion resistance and a broader passivation zone as compared with Mg, attributing to the thick corrosion products covering with the surface and the inhibition of corrosion attack. The principal cause of higher corrosion resistance of AZ91 alloy is associated with the mechanism: The aggregate network of $\beta$-phase acts as the electrochemical barrier to the progression of corrosion attack. $Al_2O_3$ and $Al(OH)_3$ compounds appeared significantly on the passivation film by XPS, indicating that the Mg matrix dissolution during the corrosion attack accompanies with the aluminium reaction on the metallic surface which improves the corrosion resistance of AZ91 alloy.

**Acknowledgments** The authors wish to thank Dr. Hideo Iwai for his technical assistance in the experiment.

## References

1. Song GL, Atrens A (2005) Proceedings of 16th International Corrosion Congress. NACE International, Beijing
2. Song GL, Atrens A, Wu XL, Zhang B (1998) Corros Sci 40:1769
3. Song GL, Atrens A, Dargusch M (1998) Corros Sci 41:249
4. Shi ZM, Song GL, Atrens A (2006) Corros Sci 48:1939
5. Ballerini G, Bardi U, Bignucolo R, Ceraolo G (2005) Corros Sci 47:2173
6. Baliga CB, Tsakiropoulos P, Jeynes C (1991) J Mater Sci 26:1497
7. Loose WS (1946) In: Pidgeon LM, Mathes JC, Woldmen NE (eds) Metals handbook. ASM International, Materials Park, p 173
8. Ambat R, Aung NN, Zhou W (2000) J Appl Electrochem 30:865
9. Pardo A, Merino MC, Coy AE, Arrabal R, Viejo F, Matykina E (2008) Corros Sci 50:823
10. Pardo A, Merino MC, Coy AE, Viejo F, Arrabal R, FeliuJr S (2008) Electrochim Acta 53:7890
11. Zhao CM, Liu M, Song GL, Atrens A (2008) Corros Sci 50:3168
12. Wu GH, Fan Y, Atrens A, Zhai CQ, Ding WJ (2008) J Appl Electrochem 38:251
13. Baliga CB, Tsakiropoulos P (1993) Mater Sci Technol 9:513
14. Song GL, Atrens A (1999) Adv Eng Mater 1:11
15. Raman RKS (2004) Metall Mater Trans A 35:2525
16. Zhang T, Shao Y, Meng G, Wang F (2007) Electrochim Acta 53:561
17. Barchiche CE, Rocca E, Juers C, Hazan J, Steinmetz J (2007) Electrochim Acta 53:417
18. Shinohara T, Wang L (2008) Proceedings of 54$^{th}$ Japan Society of Corrosion Engineering on Materials and Environments C310
19. Wang L, Shinohara T, Zhang BP (2009) Corros Eng Jpn 58:105
20. Zhao MC, Liu M, Song GL, Atrens A (2008) Corros Sci 50:1939
21. Zhao MC, Liu M, Song GL, Atrens A (2008) Adv Eng Mater 10:583
22. Shi ZM, Liu M, Atrens A (2010) Corros Sci 52:579
23. Uhlig HH, Revie RW (1985) Corrosion and corrosion control, 3rd edn. Wiley, New York
24. Lunder O, Lein JE, Hesjevik SM, Aune TKr, Nisancioglu K (1994) Mater Corros 45:331
25. Lindstr m R, Johansson LG, Thompson GE, Skeldon P, Svensson JE (2004) Corros Sci 46:1141
26. Lindstr m R, Johansson LG, Svensson JE (2003) Mater Corros 54:587
27. Burstein GT, Organ RM (2005) Corros Sci 47:2932
28. Bohni H, Uhlig HH (1969) J Electrochem Soc 116:906
29. Hazzazi OA, Zaky AM, Amin MA, Abd El Rehim SS (2008) Int J Electrochem Sci 3:489
30. Nordlien JH, Ono S, Masuko N, Nisancioglu K (1997) Corros Sci 39:1397